Chemical Engineering Science 301 (2025) 120694

Contents lists available at ScienceDirect

Chemical Engineering Science

journal homepage: www.elsevier.com/locate/ces

Numerical simulation of gasifier optimization for combined hydrogen production and carbon reduction in a chemical looping gasification (CLG) system

Junjie Lin [a], Kun Luo [a,b,*], Shuai Wang [a,b], Jianren Fan [a,b]

[a] State Key Laboratory of Clean Energy Utilization, Zhejiang University, Hangzhou 310027, China
[b] Shanghai Institute for Advanced Study of Zhejiang University, Shanghai 200120, China

ARTICLE INFO

Keywords:
Chemical looping gasification
CFD-DEM
Optimization
Hydrogen production
Carbon reduction

ABSTRACT

Chemical looping gasification (CLG) for combined hydrogen production and carbon capture represents a significant pathway for the clean, low-carbon utilization of traditional fossil fuels. Currently, a significant knowledge gap remains concerning the interplay between reactor configuration optimization and the complex gas–solid interactions in the CLG systems. This study integrates reactive computational fluid dynamics-discrete element method (CFD-DEM) simulations with a coarse-grained model (CGM) to analyze 3D coal-based CLG systems. The spatiotemporal distributions of gas–solid flow dynamics and thermochemical characteristics are revealed. It is found that increasing the gasifier height enhances fuel conversion and hydrogen production but compromises CO_2 absorption. Smaller reactor diameters induce excessively rapid gas–solid flows, leading to incomplete fuel conversion and reduced hydrogen yield, while larger diameters cause uneven flows, significantly deteriorating hydrogen production and carbon absorption efficiency. Based on the simulation findings, the optimal height-to-diameter ratio for the gasifier in a CLG system is approximately 28.8, optimizing H_2 production while maintaining efficient CO_2 absorption. Moreover, the superficial gas velocity has a multifaceted influence on the hydrogen production and carbon reduction performance in the CLG process, necessitating a comprehensive consideration of its effects on fuel reaction time, gas–solid interactions, and other factors.

1. Introduction

As global environmental challenges and climate change escalate, there is an increasing demand in the energy and chemical engineering industries for the clean and low-carbon utilization of traditional fossil fuels (Liu, 2023). Hydrogen, a crucial raw material in refining and ammonia synthesis processes, is set to emerge as an environmentally friendly fuel across various sectors, including energy, power, and transportation (Yue et al., 2021). Given the convenience of transporting and low utilization costs of solid fossil fuels, along with the role of coal as a fundamental industrial energy resource, thermally converting coal into hydrogen-rich syngas is considered a pivotal technology for the clean and efficient use of coal resources (Matamba et al., 2022). Nevertheless, CO_2 emissions from coal gasification not only impede global efforts toward carbon neutrality but also degrade the quality and value of the product syngas. Therefore, there is an urgent need to develop cost-effective and efficient carbon capture technologies.

Recent substantial efforts in the development of carbon capture, utilization, and storage (CCUS) have been directed at addressing CO_2 emissions post-fuel utilization (Han et al., 2023; Jiang and Ashworth, 2021). However, the deployment of additional equipment escalates capital costs and diminishes economic efficiency. Recently, chemical looping technology, recognized for its inherent capability of CO_2 enrichment, has been extensively applied in chemical processes such as combustion, gasification, and reforming. Integrating coal gasification and chemical looing technology facilitates the efficient production of hydrogen and reduction of carbon from fossil fuels. It is viewed as a promising solution for the efficient, clean, and low-carbon utilization of fuels (Abuelgasim et al., 2021; Cai et al., 2018; Mohamed et al., 2020). As illustrated in Fig. 1, the coal-based chemical looping gasification (CLG) system consists of a gasifier and a combustor. Coal fuel primarily undergoes pyrolysis and gasification in the gasifier, along with the capture of CO_2 through a calcium-based sorbent. The absorption of CO_2 during the gasification process not only reduces the CO_2 content in the

* Corresponding author.
E-mail address: zjulk@zju.edu.cn (K. Luo).

https://doi.org/10.1016/j.ces.2024.120694
Received 25 June 2024; Received in revised form 20 August 2024; Accepted 2 September 2024
Available online 3 September 2024

product gas yields but also enhances the H_2 generation, resulting in H_2-riched syngas at the gasifier outlet. The primary role of the combustor is to regenerate the calcium-based sorbent using the heat released from the char combustion. Thus, a high concentration of CO_2 can be obtained at the combustor outlet. The circulation of calcium-based sorbent and inert sand bed material between the two reactors facilitate the effective heat and mass transfer in the CLG process.

Chen et al. (2017) developed a cost-effective cyclic material from the alumina industrial residual for the H_2-riched syngas production via the solid-fueled CLG process by evaluating the performance of the product syngas composition and yield, char conversion rate, and solid circulation rate in a fluidized bed. The experimental results showed that the presence of alkaline metals in the bed materials enhances the catalytic functions on char gasification and syngas reforming reactions, resulting in higher hydrogen production in the CLG process. Udomsirichakorn and Salam (2014) compared the performance of traditional biomass gasification for hydrogen production without carbon absorption against the CLG process using CaO as a CO_2 absorbent, highlighting the latter as a promising, renewable, sustainable, and eco-friendly hydrogen production technique. Ismail et al. (2016) improved the performance of both chemical looping combustion (CLC) and CLG systems by mechanically incorporating CaO particles into the Fe-based oxygen carriers. Experimental results noted that adding CaO particles not only boosts hydrogen production but also enhances the circulation stability of oxygen carrier in the chemical looping systems, although the formation of $Ca_2Fe_2O_5$ during the reaction may diminish the oxygen transportation capacity. Wang et al. (2019) developed a novel absorbent for the coal-based CLG system, finding that increasing the content of CaO in the absorbent helps to enhance the lower heating value of the gas products. It is evident that current experimental investigation on the CLG process primarily focuses on the preparation of absorbent materials. However, due to limitations in measurement technique and harsh operating condition in the coal-based CLG system, experimental investigation struggle to provide thorough insights into complex physicochemical interactions within and between gas–solid phases, thereby restricting the operational control and configuration optimization of CLG system.

With ongoing advancements in computer hardware performance and algorithmic theories, computational fluid dynamics (CFD) approaches are increasingly employed as an alternative to experimental research in studying the CLG process. Li et al. (2019) numerically examined the influences of temperature, fuel particle feed rate, and gasifying agent content on the product gas yields in a CLG system by using the two-fluid model (TFM). Their results indicated that as operating temperature increases, the concentrations of H_2 and CO at the reactor outlet also rise, whereas the concentrations of hydrocarbons and CO_2 decrease. Furthermore, increasing the fuel feed rate yields more syngas but leads to a reduction in the carbon conversion rate in the CLG process. Wang et al. (2018b) utilized the TFM approach to simulate the CLG behaviors of syngas production from coal char. Numerical results demonstrate that the production of syngas in the CLG system reduces with the decrease of the inlet gas velocity. Additionally, larger bed material particle size worsens the mixing efficiency of the dispersed particles, while higher gas inlet velocity suppresses particle segregation. Shen et al. (2023) investigated the influences of superficial gas velocity, solid inventory, coal diameter on the fluidization performance in a coal-based CLG system via the multiphase particle-in-cell (MP-PIC) method. Numerical results indicated that the gas products released during the CLG process could significantly mitigate the non-uniform distribution of pressure gradient in the reactor. Wang et al. (2024) studied the effects of different operating conditions on the solid circulation rate, pressure drop, and flow dynamics in a cold-state CLG system of solid fuels using the MP-PIC approach. It was pointed that a larger gas inlet velocity and static bed height will escalate the particle attrition in the spouted bed reactor of the CLG system. Dymala et al. (2022) numerically examined the influences of operating temperature, steam/biomass ratio, and bed mass on the behaviors of syngas composition in the biomass-based CLG process by utilizing the MP-PIC approach. They found that the hydrogen concentration increases with rising temperatures due to the methane reforming reaction. In summary, current researches on CLG simulations primarily employ the TFM and MP-PIC methods, with a focus on the impact of operating conditions on gas–solid flow dynamics and gas species composition at the reactor outlet. However, due to the assumption of solid particles as a continuous phase, the TFM approach fails to provide detailed information at the particle scale. The MP-PIC method lacks a complete heat transfer mechanism and requires further enhancements to enhance its simulation accuracy due to its simplification on the solid collisions (Liang et al., 2014). The computational fluid dynamics-discrete element method (CFD-DEM) is capable of capturing detailed particle-scale information and accurately resolving solid contacts (Golshan et al., 2020; Hu et al., 2019a; Lin et al., 2022b). However, there are currently almost no simulations of coal-based CLG simulations that utilize the CFD-DEM method, due to the significant computational resources demanded by this method (El-Emam et al., 2021; Kieckhefen et al., 2020; Lu et al., 2021). Additionally, investigations into the scale-up design and configuration optimization of reactors in the CLG system is crucial for enhancing the efficiency of hydrogen production and carbon reduction in coal CLG system and its commercial application.

Therefore, the primary objective of this study is to develop a robust Eulerian-Lagrangian method capable of efficiently simulating the complex gas–solid reactive processes that involve large numbers of particles, particularly in systems such as CLG. In the current simulation, a coarse-grained model has been integrated into the reactive CFD-DEM

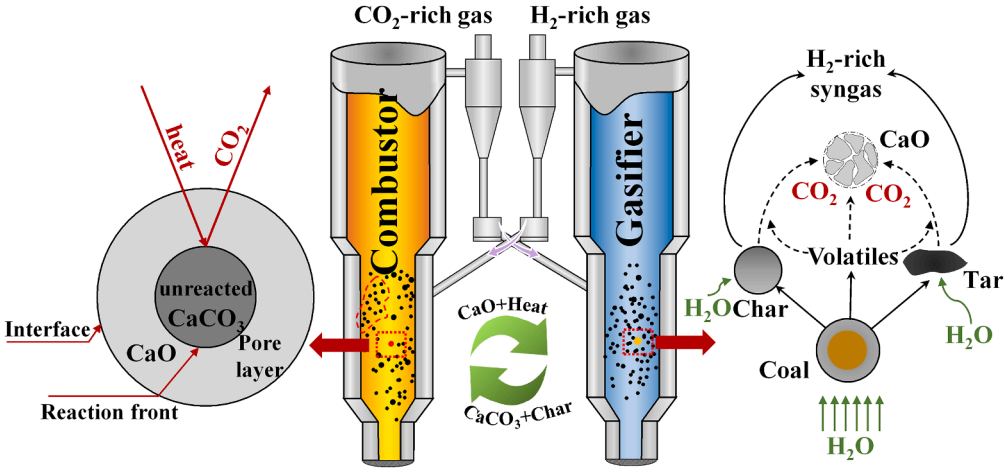

Fig. 1. Schematic diagram of the coal-based CLG system.

framework to simulate the three-dimensional (3D) coal-fueled CLG systems. The proposed reactive coarse-grained CFD-DEM is quantitatively validated against the experimental data and tested for independence analysis. The current numerical investigation specifically focuses on optimizing the structural parameters of the gasifier in the coal-fueled CLG process, aiming to elucidate how these structural configurations impact the spatiotemporal distribution of gas–solid hydrodynamics and the thermochemical performance of hydrogen production and carbon capture. These simulations promise to provide theoretical guidance and support for the fundamental understanding and scale-up optimization of reactors in the CLG process.

2. Methodology

Given the large number of sand bed material particles, coal fuel particles, and CaO absorbent particles in the 3D CLG system, a coarse-grained approach is integrated within the reactive CFD-DEM framework to boost the computational efficiency. In particular, the coarse-grained parcel (CGP) concept is applied in the current simulation to reduce computational costs by grouping together a set of original particles sharing identical physical and chemical properties (e.g., diameter, species, temperature, etc.). The reactive coarse-grained CFD-DEM method has been employed in our previous studies (Lin et al., 2023; Lin et al., 2020a) to simulate cold-state gas–solid flow and gas-fueled CLG process, demonstrating its capability to accurately predict gas–solid hydrodynamics and thermochemical characteristics during fluidization processes. The detailed mathematical models in the reactive coarse-grained CFD-DEM method for solving the gas–solid flow with heat and mass transfer, and chemical reactions are given below.

2.1. Governing equations for the gas phase

In the reactive coarse-grained CFD-DEM approach, the gas phase is treated as a continuous phase. The continuity equation, momentum conservation equation, energy conservation equation, and species transport equation, accounting for the presence of solid particles, are solved at the grid scale, as summarized in Table 1.

Here, ε_g, ρ_g, and $\boldsymbol{u}_g$ represent the voidage, gas density, and gas velocity, respectively. R_g in the continuity equation is the production or consumption of gas phase due to chemical reactions, p_g is the pressure of gas phase, τ_g is the gas stress tensor. I_{gs} in the momentum conservation equation stand for the interphase momentum exchange. C_g, T_g, and κ_g in the energy conservation equation are the specific heat capacity, temperature, and thermal conductivity of the gas phase, respectively. Q_{gs} represents the interphase convective heat transfer. ΔH_{rg} is the reaction heat. $Y_{g,i}$, $D_{g,i}$, and $R_{g,i}$ in the species transport equation stand for the mass fraction of species i, diffusivity coefficient, and the consumption or generation of species i due to chemical reactions, respectively. More detailed description can refer to our previous studies (Lin et al., 2023; Wang and Shen, 2022).

Table 1
Governing equations for the gas phase in the reactive coarse-grained CFD-DEM.

Equations	Formulations	Eq.
Mass conservation	$\frac{\partial}{\partial t}(\varepsilon_g\rho_g) + \nabla\cdot(\varepsilon_g\rho_g\boldsymbol{u}_g) = R_g$	(1)
Momentum conservation	$\frac{\partial}{\partial t}(\varepsilon_g\rho_g\boldsymbol{u}_g) + \nabla\cdot(\varepsilon_g\rho_g\boldsymbol{u}_g\boldsymbol{u}_g) = -\varepsilon_g\nabla p_g + \varepsilon_g\rho_g\boldsymbol{g} + \nabla\cdot(\varepsilon_g\tau_g) - I_{gs}$	(2)
Energy conservation	$\frac{\partial}{\partial t}(\varepsilon_g\rho_g C_g T_g) + \nabla\cdot(\varepsilon_g\rho_g\boldsymbol{u}_g C_g T_g) = \nabla\cdot(\varepsilon_g\kappa_g\nabla T_g) - Q_{gs} - \Delta H_{rg}$	(3)
Species conservation	$\frac{\partial}{\partial t}(\varepsilon_g\rho_g Y_{g,i}) + \nabla\cdot(\varepsilon_g\rho_g\boldsymbol{u}_g Y_{g,i}) = \nabla\cdot(\varepsilon_g\rho_g D_{g,i}\nabla Y_{g,i}) + R_{g,i}$	(4)

2.2. Governing equations for the solid phase

The solid motion and thermochemical properties are tracked individually under the Lagrangian framework in the reactive coarse-grained CFD-DEM. The coarse-grained parcel (CGP) concept is employed to reduce computational costs. The diameter and mass relationship between a CGP and an original particle can be formulated as:

$$d_{CGP} = kd_p = W^{1/3}d_p \tag{5}$$

$$m_{CGP} = k^3 m_p = W m_p \tag{6}$$

where d_{CGP} and d_p represent the diameter of the CGP and original particle, respectively. m_{CGP} and m_p represent the mass of the CGP and original particle, respectively. W is the statistical weight of the original particle in a specific CGP, while k is the coarse-grained ratio. Specifically, the evolution of solid motion, temperature, mass, and species characterized at CGP scale are given in Table 2.

Here, $\boldsymbol{v}_{CGP}$ and $\boldsymbol{\omega}_{CGP}$ are the velocity and angular velocity of the CGP, respectively. $\boldsymbol{F}_d$, $\boldsymbol{F}_p$, and $\boldsymbol{F}_c$ in the translational motion equation represent the drag force between CGP and gas phase, pressure gradient force, and collision force between CGP-CGP and CGP-wall, respectively. I_{CGP} and $\boldsymbol{T}_{CGP}$ in the rotational motion equation are the inertia moment and total torque acting on the calculated CGP, respectively. T_{CGP} and c_{CGP} stand for the temperature and specific heat capacity of the current CGP. Moreover, the interphase convective heat transfer $Q_{gp,CGP}$, inter-CGP/CGP-wall conductive heat flux $Q_{cond,CGP}$, radiative heat exchange with surrounding environment $Q_{rad,CGP}$, and reaction heat $Q_{react,CGP}$ are comprehensively considered in the energy equation. R_{sn} means the consumption/production rate of species n (Y_n) in the reactive CGP.

2.3. Sub-models implementation

Chemical looping gasification encompasses intricate physicochemical processes. In order to accurately reproduce the gas–solid hydrodynamics and heat and mass transfer characteristics in the coal-fueled chemical looping gasification, an interphase momentum exchange coefficient considering the polydispersity influence, the soft-sphere collision model suitable for frequent multi-body contacts, various heat transfer mechanisms (i.e., convection, conduction, radiation, and reaction), homogeneous and heterogeneous chemical reactions are thoroughly integrated into the current simulation for a comprehensive understanding. Therefore, the detailed sub-models are summarized.

2.3.1. Interphase momentum exchange

The drag force caused by the velocity difference between the specific CGP and gas can be formulated as:

$$\boldsymbol{F}_d = k^3\frac{V_{p,i}\beta}{(1-\varepsilon_g)}(\boldsymbol{u}_g - \boldsymbol{v}_{p,i}) \tag{12}$$

where β denotes the interphase momentum exchange coefficient, which

Table 2
Governing equations for the solid phase in the reactive coarse-grained CFD-DEM.

Equations	Formulations	Eq.
Translational motion	$m_{CGP}\frac{d\boldsymbol{v}_{CGP}}{dt} = m_{CGP}\boldsymbol{g} + \boldsymbol{F}_d + \boldsymbol{F}_p + \boldsymbol{F}_c$	(7)
Rotational motion	$I_{CGP}\frac{d\boldsymbol{\omega}_{CGP}}{dt} = \boldsymbol{T}_{CGP}$	(8)
Energy equation	$m_{CGP}c_{CGP}\frac{dT_{CGP}}{dt} = Q_{gp,CGP} + Q_{cond,CGP} + Q_{rad,CGP} + Q_{react,CGP}$	(9)
Mass equation	$\frac{dm_{CGP}}{dt} = \sum_{n=1}^{N_s} R_{sn}$	(10)
Species equation	$\frac{dY_n}{dt} = \frac{1}{m_{CGP}}(R_{sn} - Y_n\sum_{n=1}^{N_s} R_{sn})$	(11)

is assessed at the original particle scale. The total drag force acting on a specific computational parcel is computed as the sum of the drag forces experienced by the k^3 original particles it represents. Due to the presence of various complex solid particles in the coal CLG system (i.e., coal particles, oxygen carrier particles, and sand), it is necessary to consider the influence of particle polydispersity on the hydrodynamics and thermochemical properties of gas–solid flow. In the current simulation, a polydispersion correction factor initially introduced by Beetstra et al. (2007a, b) is employed to address the interphase momentum exchange between gas and complex solid particles. The polydispersed drag model which has been extensively validated in our previous simulations involving solid mixing (Lin et al., 2020b), coal gasification (Hu et al., 2019b), and chemical looping combustion (Lin et al., 2023) in fluidized beds is detailed in Table 3.

2.3.2. Solid collisions

In the CLG system, frequent and substantial collisions occur among solid particles. Solid collisions play a pivotal role in shaping the overall behavior and dynamics of the particulate system within the CLG process. Generally, two primary solid contact models are commonly employed in the simulation, namely the hard-sphere model and the soft-sphere model. The hard-sphere model utilizing an event-driven algorithm assumes instantaneous and binary collisions between particles. On the other hand, the soft-sphere model introduces a time-driven scheme, allowing for continuous, time-dependent collisions and accommodating a more realistic representation of multiple interactions between particles over time. Therefore, the linear spring-dashpot (LSD) collision model, grounded in the principle of the soft-sphere model, is utilized to enhance the accuracy current simulation. Specifically, the calculation of collision forces in the coarse-grained CFD-DEM is performed at the CGP scale and can be decomposed into two main components: a normal component ($\boldsymbol{F}^n_{c,ij}$) and a tangential component ($\boldsymbol{F}^t_{c,ij}$). As formulated in Eqs. (21) and (22), there are mainly two key parameters in this model: spring constants (k_n, k_t) and damping coefficients (η_n, η_t). The spring constant represents the stiffness of the "spring" in the model while the damping coefficient accounts for the energy dissipation during the collision. The spring constant and damping coefficient are usually assumed to be identical between the original particle system and the coarse-grained system in previous investigations (Mori and Sakai, 2021; Sakai et al., 2014; Xie et al., 2020). It is important to note that the introduction of the CGP concept reduces the collision frequency among computational parcels compared to the original particles in the CLG system, leading to inconsistencies in energy dissipation between the coarse-grained system and the original system (Lu et al., 2017a; Lu et al., 2017b; Wang and Shen, 2022). Therefore, an effective restitution coefficient (Eq. 23) is employed in the present simulation to address this computational discrepancy (Lu et al., 2014). Table 4 summaries the details of the collision model implemented in this study.

Table 3
Interphase momentum exchange model used in the present simulation.

Formulations	Eq.
Drag model for the monodispersed system of dense and dilute phases: $\beta_{mono} = \begin{cases} \frac{3}{4}C_D\frac{\rho_g\varepsilon_g(1-\varepsilon_g)\lvert\boldsymbol{u}_g-\boldsymbol{v}_{p,i}\rvert}{\langle d\rangle}\varepsilon_g^{-2.65} & \varepsilon_g \geq 0.8 \\ \frac{150(1-\varepsilon_g)^2\mu_g}{\varepsilon_g\langle d\rangle^2}+\frac{1.75\rho_g(1-\varepsilon_g)\lvert\boldsymbol{u}_g-\boldsymbol{v}_{p,i}\rvert}{\langle d\rangle} & \varepsilon_g < 0.8 \end{cases}$	(13)
Single-particle drag coefficient in the free flow: $C_D = \begin{cases} \frac{24(1+0.15Re_{p,i}^{0.687})}{Re_{p,i}} & Re_{p,i} < 1000 \\ 0.44 & Re_{p,i} \geq 1000 \end{cases}$	(14)
Particle Reynolds number: $Re_{p,i} = \frac{\rho_g\varepsilon_g\lvert\boldsymbol{u}_g-\boldsymbol{v}_{p,i}\rvert d_{sm}}{\mu_g}$	(15)
Interphase momentum exchange coefficient for polydispersed system: $\beta = f_{p,i}\beta_{mono}$	(16)
Polydispersion correction factor: $f_{p,i} = 0.064\varepsilon_g y_i^3 + (1-\varepsilon_g)y_i^2 + \varepsilon_g y_i$	(17)
Dimensionless parameter: $y_i = \frac{d_{p,i}}{\langle d\rangle}$	(18)
Sauter mean diameter: $\langle d\rangle = \frac{\sum_{i=1}^{c} N_i d_{p,i}^3}{\sum_{i=1}^{c} N_i d_{p,i}^2}$	(19)

2.3.3. Heat transfer model

It is assumed that the temperature of a specific computational parcel is uniformly distributed. Specifically, the Gunn's Nusselt number (Nu_p) correlation (Gunn, 1978) is adopted for the calculation of gas–solid convection ($Q_{gp,CGP}$). The Batchelor and O'Brien's contact conduction ($Q_{pp,CGP}$) mechanism (Batchelor and O'Brien, 1977) and the Rong and Horio's non-contact conduction ($Q_{pfp,CGP}$) mechanism (Rong and Horio, 1999) are both considered in the current simulation. The radiative heat transfer ($Q_{rad,CGP}$) for a specific CGP with its surrounding environment temperature (T_{env}) is calculated with the P-1 radiative model. The reaction heat ($Q_{react,CGP}$) due to chemical reactions is calculated through the enthalpy (H) change between products and reactants. Table 5 gives the details of the heat transfer model considered in the current simulation.

2.3.4. Chemical reactions

A series of complex chemical reactions take place in the CLG system. There are two types of reactive particles in the CLG process: solid fuel coal and calcium-based sorbent. Additionally, inert sand particles are selected as bed material to enhance the heat and mass transfer efficiency and uniformity in the CLG system. Table 6 presents the summary of chemical reactions considered in the gasifier of CLG system. Upon entering the CLG system, coal particles undergo rapid heating to facilitate moisture evaporation (R1), followed by coal pyrolysis (R2) to release volatiles. In the current simulation, reactions involving nitrogen and sulfur are not taken into account due to their little amount. Specifically, a composition of H_2, CO, CH_4, CO_2, and H_2O are considered for the volatiles, with the coefficients of each species determined based on the element conservation by the proximate and ultimate analysis (Wang et al., 2014). Subsequently, the resulting char undergoes gasification (R3, R4) with high-temperature gasification agents to produce H_2 and CO. Furthermore, intense steam-methane reforming (SMR, R6) and water–gas shift (WGS, R7) reactions take place within the gasifier. CO_2 generated during the CLG process is absorbed and fixed by the calcium-based sorbent to form $CaCO_3$, consequently promoting WGS reaction towards hydrogen production, thereby augmenting both H_2 yield and content.

The chemical reaction rates of drying process can be expressed as the first-order Arrhenius form (Bryden et al., 2002):

$$r_1 = 5.13\times10^{10}\exp(-88000/RT_p)[H_2O(l)] \tag{31}$$

Table 4
LSD collision model in the reactive coarse-grained CFD-DEM.

Formulations	Eq.
Collision force exerting on a specific CGP: $\boldsymbol{F}_c = \boldsymbol{F}^n_{c,ij} + \boldsymbol{F}^t_{c,ij}$	(20)
Normal collision force: $\boldsymbol{F}^n_{c,ij} = -(k_n\delta_n)\boldsymbol{n} + (\eta_n\dot{\delta}_n)\boldsymbol{n}$	(21)
Tangential collision force: $\boldsymbol{F}^t_{c,ij} = \min[\left(-k_t\delta_t + \eta_t\dot{\delta}_t\right)\boldsymbol{t}, \mu_{CGP}\boldsymbol{F}^t_{c,ij}]$	(22)
Effective restitution coefficient: $e_{CGP} = \sqrt{1+(e_p^2-1)k}$	(23)
Damping coefficient: $\eta_n = \sqrt{2k_n m_{CGP,eff}}\ \frac{\lvert\ln e_{CGP}\rvert}{\sqrt{\pi^2+\ln^2 e_{CGP}}}$	(24)

Table 5
Heat transfer mechanisms considered in the simulation of the CLG process.

Formulations		Eq.
Convection:	$Q_{gp,CGP} = \pi d_p Nu_p \kappa_f (T_f - T_p) k^3$	(25)
	$Nu_p = \left(7 - 10\varepsilon_g + 5\varepsilon_g^2\right)\left(1 + 0.7Re_{p,i}^{0.2}Pr^{0.33}\right) + \left(1.33 - 2.4\varepsilon_g + 1.2\varepsilon_g^2\right)Re_{p,i}^{0.7}Pr^{0.33}$	(26)
Contact conduction:	$Q_{pp,CGP} = \frac{4R_{c,ij}(T_{p,j} - T_{p,i})}{(1/\kappa_{p,i} + 1/\kappa_{p,j})}\left(\frac{f(e_{CGP})}{f(e_p)}\right)^{1/2} k^4$	(27)
Non-contact conduction:	$Q_{pfp,CGP} = \kappa_g (T_{p,j} - T_{p,i}) k^2 \int_{R_{in}}^{R_{out}} \frac{2\pi r}{l_{ij} - \left(\sqrt{R_{p,i}^2 - r^2} + \sqrt{R_{p,j}^2 - r^2}\right)} dr$	(28)
Radiation:	$Q_{rad,CGP} = \sigma A_p \varepsilon_p \left(T_{env}^4 - T_p^4\right) k^3$	(29)
Reaction heat:	$Q_{react,CGP} = -\frac{dm_p}{dt}(H_{products} - H_{reactants}) k^3$	(30)

Table 6
Chemical reactions considered in the current simulation.

Heterogeneous reactions	
$H_2O(l) \rightarrow H_2O(g)$	R1
Volatiles$\rightarrow \alpha_1 CO + \alpha_2 CO_2 + \alpha_3 H_2 + \alpha_4 H_2O + \alpha_5 CH_4$	R2
$C + H_2O \rightarrow CO + H_2$	R3
$C + CO_2 \rightarrow 2CO$	R4
$CaO + CO_2 \leftrightarrow CaCO_3$	R5
Homogeneous reactions	
$CH_4 + H_2O \rightarrow CO + 3H_2$	R6
$CO + H_2O \leftrightarrow CO_2 + H_2$	R7

The widely used METC Gasifier Advanced Simulation (MGAS) model is employed to determine the kinetic parameters of coal pyrolysis (Hu et al., 2019b; Yu et al., 2020; Yu et al., 2021).

$$r_2 = 1.1 \times 10^5 \exp(-88700/RT_p) m_p (X_{VM} - X^*)/MW_{VM}$$
$$X^* = \begin{cases} \left(\frac{867.2}{T_p - 273}\right)^{3.914}/100 & T_p > 273 \\ 0 & T_p \le 273 \end{cases} \quad (32)$$

The char gasification is a typical surface reaction. In this study, a kinetic/diffusion-limited rate model (Baum and Street, 1971; Wang et al., 2020) is employed to represent the reaction rates of R3 and R4, which simultaneously consider the diffusion and reaction effects of the gasifying agent on the char surface.

$$r_{C,i} = -A_i p_i / [(1/r_{diff,i} + 1/r_{kin,i}) MW_C]$$
$$r_{diff,i} = C_i \frac{[(T_p + T_g)/2]^{0.75}}{d_p} \quad r_{kin,i} = A_i T_p \exp(-E_i/RT_p) \quad (33)$$

The pre-exponential factors (A_i) of R3 and R4 are 45.6 and 8.3 s/mK, respectively. The activation energy (E_i) for R3 and R4 is set to 43.7 kJ/mol. C_i and p_i are the mass diffusion constant and gasification agent partial pressure, respectively.

In the current simulation, the carbonation (R5f) and calcination (R5r) configurations vary depending on conditions of CO_2 fraction and operating temperature. The correlation proposed by Baker (1962) is employed for the determination of equilibrium CO_2 concentration over CaO ($C_{CO2,eq}$):

$$C_{CO_2,eq} = \frac{1.462 \times 10^{11}}{T} \exp(-19130/T) \quad (34)$$

The semiempirical chemical reaction rate of R5f is expressed as (Fang et al., 2009):

$$r_{5f} = K_{carb}(1 - X_{carb}/X_u)^{2/3}(C_{CO_2} - C_{CO_2,eq})^{(P/P_0)^{0.083}}$$
$$X_u = 0.1097(T/100) - 0.3391 \quad (35)$$

where K_{carb} and X_u represent the apparent rate constant and apparent kinetic expression of CaO carbonation, respectively. X_{carb} is the conversion of the calcium-based sorbent.

The chemical reaction rate of R5r is given as (Fang et al., 2009):

$$r_{5r} = K_{calc}(1 - X_{calc})^{2/3}(C_{CO_2,eq} - C_{CO_2})$$
$$K_{calc} = k_{0,calc} \exp(-150000/RT_p) \quad (36)$$

The kinetic parameters of homogeneous reactions are listed in Table 7.

3. Computational details

The investigated CLG unit in the current simulation is based on the experimental setup conducted by Wang et al. (2014). Fig. 2 displays the schematic diagram of the fluidized bed gasification apparatus in the CLG system, which mainly consists of a fluidized bed gasifier, a feedstock hopper, a cyclone, a steam preheater, and a gas cleaning and sampling system, etc. In the CLG system, coal is deployed as the solid fuel for the production of syngas, while CaO serves as the carbon carrier for the absorption of CO_2 generated during the gasification process. Sand is utilized as an inert bed material, facilitating the uniformity of system mixing and thermochemical transfer efficiencies. Steam generated by the steam generator is injected at the bottom of the gasifier to fluidize the bed material and act as a gasification agent. Upon introduced into the CLG system, coal particles undergo a sequence of physical and chemical processes including drying, pyrolysis, gasification, homogeneous and heterogeneous chemical reactions. The CO_2 emitted from the gasification process is absorbed by CaO, leading to the formation of $CaCO_3$. The gas and solid product yields are then directed to the cyclone for separation, culminating in the extraction of H_2-enriched syngas product at the outlet of the gasifier. Simultaneously, the generated $CaCO_3$ is conveyed to a calcination combustor for regeneration and recycling.

The current numerical investigation primarily focuses on the gasifier, examining its performance in hydrogen production and carbon dioxide capture with various reactor structures. The inner diameter and height of gasifier are 66 mm and 2300 mm, respectively. To maintain consistency with the experimental setup, a premixture of coal and CaO is utilized as the mass inlet feedstock for the CLG simulation, with an initial static bed mass of 1 kg of quartz sand serving as the bed material. The calcium/carbon and steam/carbon ratios are respectively set at 1:1 and 2:1, with the operating temperature of gasifier established at 1023 K. The proximate and ultimate analyses of the Ningxia bituminous coal with an average diameter of 170 μm are presented in Table 8. The average particle size of calcium-based sorbent is selected to be 170 μm, containing 95.52 % Cao, with the residual components including MgO, SiO_2, Al_2O_3, among others. Giving the negligible concentrations of other chemical constituents, the current simulation primarily considers the reaction between CaO and CO_2. The average particle size for the quartz sand is selected at 150 μm. The gasifier inlet is specified as a mass inlet, while the outlet is configured to match atmospheric pressure condition, and the wall of gasifier is treated as no-slip boundary condition. The coal feed rate at the reactor inlet is regulated to 1 kg/h while the steam preheated to 700 °C with a flow rate of 1.8 kg/h is employed. The friction coefficient of solid phase is fixed at 0.3, with a spring constant of 800 N/m, and a restitution coefficient of 0.9. The finite volume method (FVM) is utilized for discretizing the governing equations of continuity,

Table 7
Reaction rates of homogeneous reactions.

Reaction rate	Eq.
$r_6 = 3.0 \times 10^{11} \exp(-126000/RT_p)[CH_4][H_2O]$	(37)
$r_{7f} = 2.78 \times 10^6 \exp(-12600/RT_p)[CO][H_2O]$	(38)
$r_{7r} = 9.59 \times 10^7 \exp(-46600/RT_p)[CO_2][H_2]$	(39)

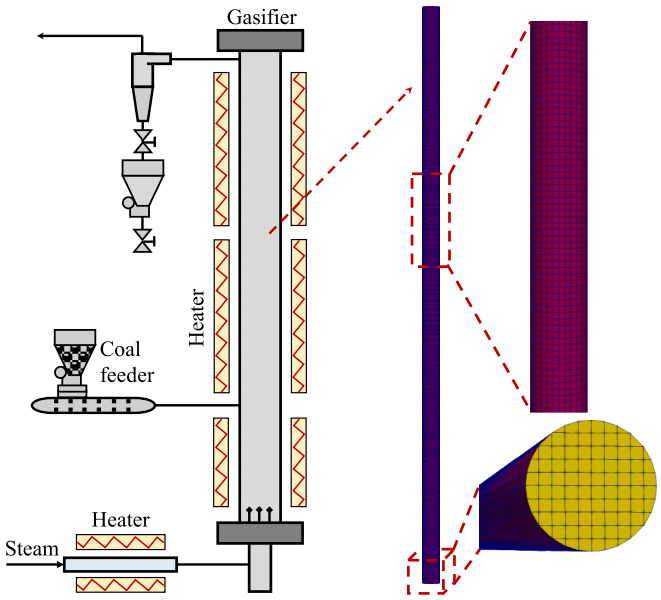

Fig. 2. Schematic diagram of gasifier in the CLG system and computational grid representation.

momentum, energy, and species. To couple the gas phase's pressure and velocity, a SIMPLE algorithm is employed. The first-order Euler scheme is utilized for the integration of the transient term and the iteration of the physicochemical characteristics of discrete particles. The solid and gas time steps adopted in the current simulations are 1×10^{-6} s and 1×10^{-5} s, respectively. The total physical time of each case modeled in this study is 20 s.

4. Results and discussion

4.1. Model validation and independence analysis

It is necessary to validate the reaction model before proceeding with the optimization and scale-up design of the gasifier in the CLG system. Considering the gasifier houses an exceedingly large number of real particles, with the static accumulation of quartz sand particles estimated between 200 and 300 million. This quantity far exceeds the computational capabilities of conventional CFD-DEM approach. Therefore, the coarse-grained CFD-DEM methodology based on the computational parcel concept is employed in the current simulation. Specifically, this approach packs the original coal particles, CaO particles, and quartz sand particles into coarse-grained parcels to accelerate the computational efficiency. To assess the influence of different coarse-grained ratios (k) on the prediction results of the CLG process, independence analysis is conducted using three different sets of CGPs with coarse-grained ratios of 10, 12, and 15.

Fig. 3(a) illustrates the time evolution of the molar fraction of the CLG product gas species. It can be observed that the concentrations of the gaseous products fluctuate around a fixed value, indicating that a quasi-equilibrium state has been achieved in the simulated gasifier. Specifically, the time-averaged molar fraction of H_2 over the time periods of 5–20 s, 10–20 s, and 15–20 s are 72.86 %, 72.18 %, and 71.98 %, respectively, with an absolute error of less than 1 % across these statistical time periods. To ensure the reliability and stability of the time-averaged results, the last 10 s of the numerical simulation are used for statistical analysis in this study. Fig. 3(b) displays a comparative analysis of the gas species concentrations at the gasifier outlet across various coarse-grained ratios against the experimental measurement. It is observed that the concentration of H_2 constitutes the majority of the flue gas at the gasifier outlet. Meanwhile, attributing to the CO_2 absorption during the CLG reactions by the CaO, a relatively low CO_2 content can be observed at the product gas yield. Additionally, the gas compositions at the outlet of the CLG gasifier modeled under different coarse-grained ratios show a close alignment with the experimental data. With the coarse-grained ratio at 10, the maximum discrepancy between the

Table 8
Proximate and ultimate analyses of the Ningxia bituminous coal.

Coal	Proximate analysis (%)				Ultimate analysis (%)				
	M	V	A	FC	C	H	O	N	S
bituminous	5.83	26.18	16.89	51.1	62.24	3.56	9.9	0.85	0.73

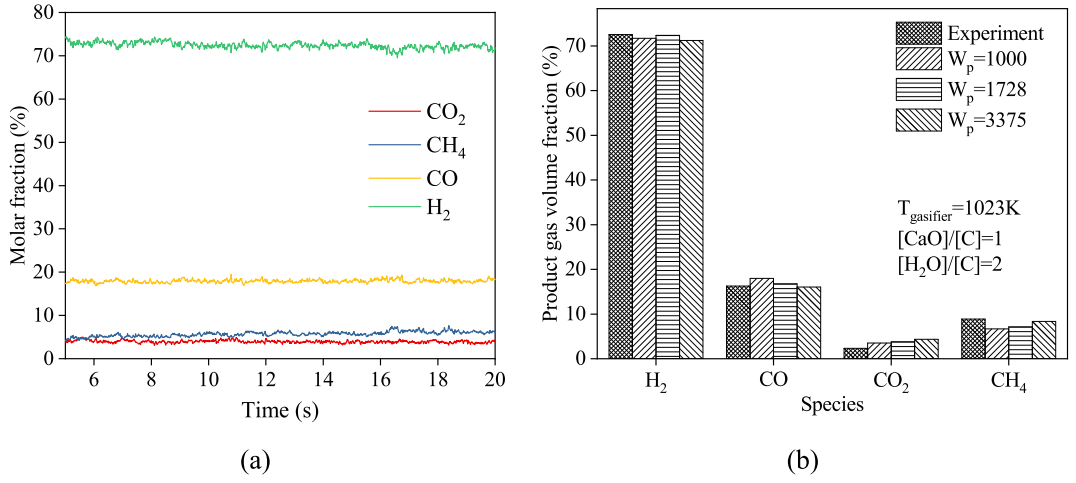

Fig. 3. Product gas species molar fractions at the gasifier outlet: (a) time evolution profile; (b) time-averaged gas species volume fractions with various coarse-grained ratios.

numerical simulation and experimental results is approximately 25 %. When the coarse-grained ratio is increased to 12, the largest deviation with experimental measurements reaches about 45 %. When a coarse-grained ratio of 15 is employed, the maximum error escalates to approximately 65 %. Such discrepancies are predominantly associated with the prediction of CO_2 and CH_4 gas components, where the relative low concentrations of these components at the flue gas result in significantly higher relative percentage errors with the experimental observations. However, for the objective gaseous products such as H_2 and CO, which have relatively higher concentrations, the discrepancies between the numerical simulations and experimental outcomes are maintained within 10 %. Consequently, it can be concluded that the numerical simulations accurately predict the contents of H_2-riched syngas at the gasifier outlet of CLG process, with prediction discrepancies falling within a tolerable range for computational inaccuracies. To balance computational precision and efficiency, a coarse-grained ratio of 12 is adopted for subsequent simulations. In addition to evaluating model accuracy, the computation times for different coarse-grained ratios are quantitatively analyzed. Specifically, using 60 CPU cores to simulate 20 s of physical time in the coal-fueled CLG process, the computation times for coarse-grained ratios of 10, 12, and 15 are 32.63 h, 17.32 h, and 14.27 h, respectively. Therefore, a coarse-grained ratio of 12 is adopted for subsequent simulations to balance computational precision and efficiency.

The computational domain is discretized using structured hexahedral grids to enhance the computational stability in the current simulation. To assess the influence of grid resolution on the computational results, a grid independence test is conducted. Utilizing a coarse-grained ratio of 12, computational meshes with size of 6 mm, 8 mm, and 10 mm are selected to represent fine, medium, and coarse grids, respectively. Fig. 4 illustrates the distribution of H_2 molar concentration along the axial height of the riser across different grid resolutions. It is observed that the concentration of H_2 increases with the height of the gasifier, attributing to the ongoing coal pyrolysis and char gasification during their ascent in the reactor, thereby progressively increasing the H_2 production. Moreover, the increment rate of H_2 concentration at the bottom of the gasifier is notably higher than in the upper regions. This distinct characteristic is due to the denser gas–solid flow at the bottom region, leading to higher gas–solid interaction efficiency and faster reaction rates. Conversely, the reaction pace is moderated due to the reduced concentrations of solid phase and reactant contents in the upper sections. Overall, the axial distributions of H_2 obtained from simulations using fine and medium grids are in close agreement, whereas the result derived from the coarse grid exhibits noticeable differences from the former two. Therefore, for an optimal compromise between computational efficiency and simulation accuracy, the medium grid size has been determined as the preferred choice for grid resolution in the following investigations.

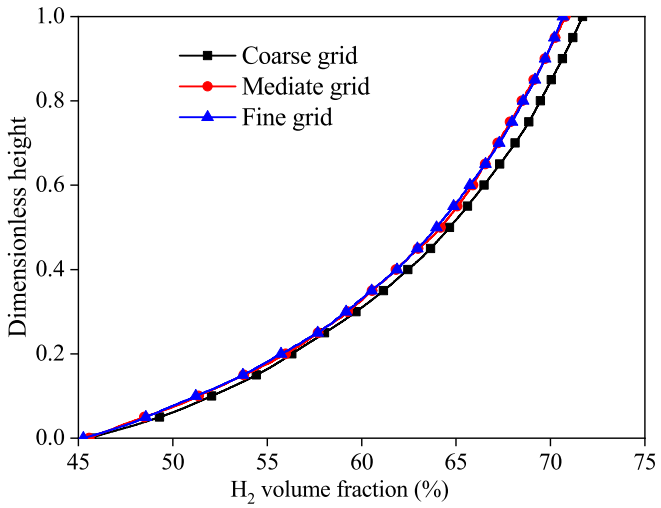

Fig. 4. Axial distributions of H_2 concentration with different grid resolutions.

4.2. Gas-solid flow pattern

The macroscopic gas–solid flow dynamic characteristics play a significant influence on the heat transfer and the chemical reactions in the gasifier of the CLG process. Fig. 5 displays the velocity distribution of solid phase from the initial moment to the attainment of steady-state flow in the CLG process. Initially, computational parcels are statically accumulated at the bottom of the gasifier. As the gasification agent is injected from the bottom of the riser, the bed materials begin to expand due to the drag force exerted from the fluid phase, causing the mass of solid parcels to ascend along the riser reactor. It is noted that the solid parcels accumulating at the surface of the bed materials exhibit higher velocities, facilitating their continuous ascent and eventually throughout the entire gasifier. As the solid parcels ascent, some exhibit a downward negative velocity near the walls, showcasing the typical particle backflow phenomenon inherent to the fluidization process. Once the gasifier becomes fully charged with bed materials, the CLG system displays a distinct concentration gradient with denser at the bottom zones and more dilute towards the top regions. Moreover, the backflow phenomenon becomes increasingly pronounced within the bottom zones of the gasifier. Furthermore, computational parcels within the central region of the riser demonstrate a noticeable upward positive velocity, characterizing the typical core-annular flow pattern commonly observed in the riser reactor.

Additionally, the distribution of gas species product concentrations in the reactor serves as an excellent indicator of the overall performance hydrogen production and carbon reduction in the CLG system. Fig. 6 depicts the spatial distribution of H_2 and CO_2 concentrations over time after achieving a stable flow state in the CLG process. Generally, the concentration of H_2 surpasses that of CO_2 by approximately an order of magnitude. Meanwhile, a relatively lower concentration of the H_2 product can be observed at the bottom of the gasifier due to the coal fuel

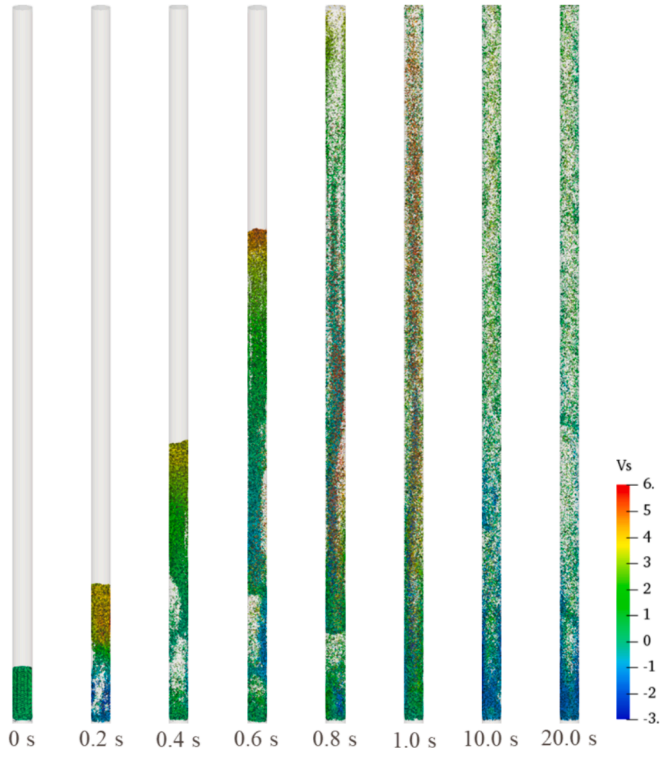

Fig. 5. Transient particle velocity distribution during the CLG process.

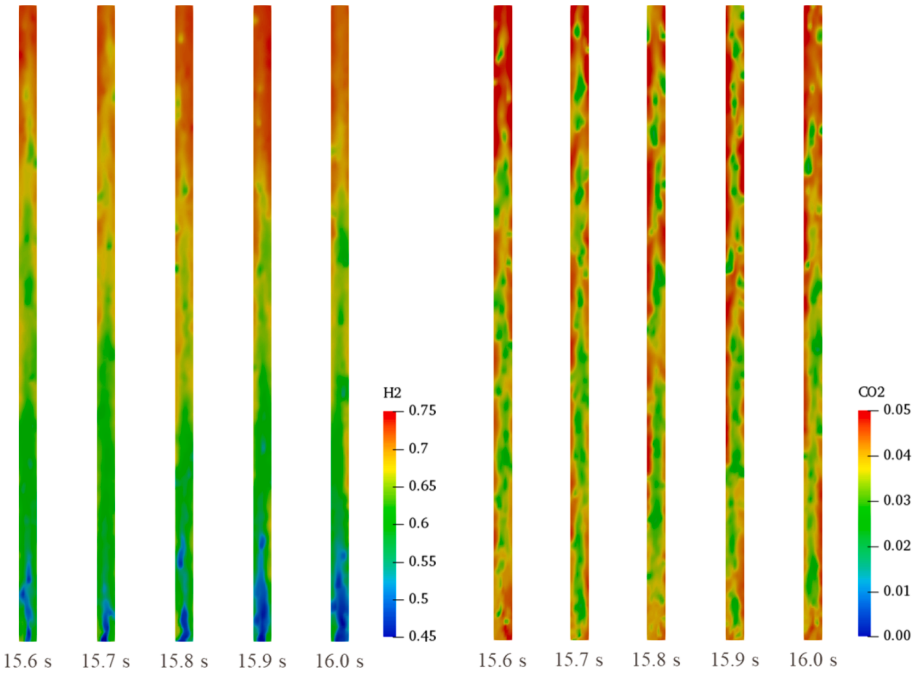

Fig. 6. Instantaneous contour plots of H_2 and CO_2 concentrations in the gasifier.

undergoing a requisite heating and evaporation process upon their initial introduction into the gasifier. As they move upward in the riser, H_2 generated from pyrolysis, gasification and homogeneous reactions progressively fills the reactor. It is also observed that the concentration of H_2 near the walls is noticeably higher than in the central region of the gasifier. This is attributed to the implementation of constant wall temperature boundary condition and no-slip boundary condition for gas phase flow in the simulation. When the gas species encounter the high-temperature walls, these conditions facilitate the forward reactions of the homogeneous reactions R6 and R7, consequently augmenting the generation of H_2. In contrast, the distribution of CO_2 concentration significantly diverges from that of H_2. Since CO_2 generated in the CLG system is absorbed by the CaO sorbent, its overall concentration in the reactor is relatively lower, generally displaying higher concentrations in the upper regions than in the lower parts of the gasifier. This pattern arises from the diminished concentration of the CaO sorbent in the upper areas of the riser, weakening the absorption efficiency of CO_2. Interestingly, the CO_2 concentration in the riser exhibits pronounced spatial nonuniform, characterized by distinct cluster formations. This is because the CaO sorbent in the gasifier is not uniformly distributed, and the formation of cluster is a characteristic feature of particle distribution in the riser reactors. Consequently, the absorption efficiency of CO_2 is significantly influenced by the clusters, resulting in the noted inhomogeneity in CO_2 concentration distribution.

4.3. *Influence of gasifier height on the CLG process*

The circulating fluidized bed (CFB) technology is garnering increased attention in the power and energy engineering owing to its high gas–solid interaction efficiency and large capacity features (Abdelmotalib et al., 2015; Wang and Zhu, 2016; Wei et al., 2020). The riser reactor stands as a critical component in systems equipped with CFB units, including chemical looping gasification, chemical looping combustion, biomass gasification, and combustion processes. Serving as the primary site for gas–solid interactions, heat and mass transfer, along with a substantial portion of the chemical reactions, the riser reactor's role is indispensable. Therefore, the configuration optimization of the riser reactor is vital for enhancing the comprehensive performance of the CLG systems. Hu et al. (2009) conducted cold-state experimental investigations of riser reactors with different heights, discovering that increasing the height of the riser reactor increases the saturation carrying capacity and the pressure drop in the system. It is well-established that as the height of the reactor increases, the residence time of fuel particles within the riser also extends, thereby enhancing the fuel conversion rate. However, the influence of riser height on the hydrogen production and carbon capture efficiency in the CLG systems necessitates further investigation and exploration. Therefore, this study numerically investigated the impact of riser height on the thermochemical characteristics in the coal-based CLG process. Table 9 presents the riser dimensions for the cases modeled in the current study. Fig. 7 shows the gas product yields at the outlet of the CLG gasifier under three sets of riser heights. The case in red label represents the base case established from experimental configurations, while the other two scenarios preserve the same inner diameter of the riser reactor but extend its height to 1.5 and 2 times that of the base case, respectively. Initial conditions and boundary conditions for each case are consistent with the base case. The numerical results conclusively show that increasing the height of the riser leads to a higher concentration of H_2 and CO_2, while simultaneously reducing the yields of CH_4 and CO. This is attributed to the extended residence time of fuel parcels in the riser as its height increases, enhancing the fuel conversion efficiency. Additionally, the increased reaction time of homogeneous reactions like SMR and WGS reactions facilitate the conversion of both CH_4 and CO into H_2. Meanwhile, with the riser height increases, the concentration of CaO in the upper sections of the riser diminishes, which hinders the adsorption and removal of CO_2 generated during the reaction, consequently increasing the CO_2 concentration at the gasifier outlet.

Fig. 8 illustrates the axial distribution of H_2 and CO_2 concentrations in the gasifier of the CLG system with different heights. To facilitate a more intuitive comparison of the gasifier heights on the hydrogen

Table 9
Riser dimensions with different heights.

case	Inner diameter (m)	Height (m)
Case_D1H1.0	0.066	2.3
Case_D1H1.5	0.066	3.45
Case_D1H2.0	0.066	4.6

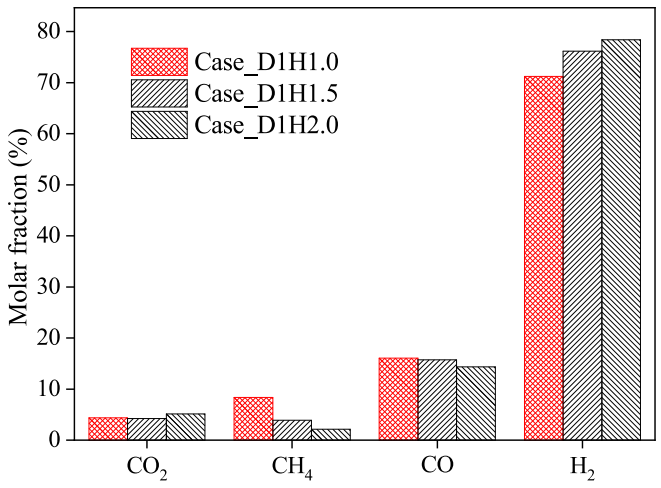

Fig. 7. Molar fractions of gas products at the outlet of risers with different heights.

production and carbon reduction in the CLG process, a dimensionless height is presented here. It can be observed that the concentration of H_2 consistently increases along the height of the riser in the CLG systems of different gasifier heights. Conversely, the CO_2 concentration shows a pattern of initial decrease followed by a gradual increase. This phenomenon is due to the initial production of CO_2 from pyrolysis upon the introduction of coal into the CLG system. Subsequently, as the CO_2 ascends, it participates in the gasification reaction and is absorbed by the CaO sorbent in the CLG system, leading to a decrease in its concentration. Nonetheless, as the height of the riser reactor increases, the gas–solid interaction efficiency between CO_2 and both char and CaO parcels in the upper region of the reactor declines, thereby deteriorating the conversion and absorption of the generated CO_2. Moreover, when the height of the gasifier is increased to twice that of the base case, a notable increase in CO_2 concentration can be observed at the gasifier outlet. This can be attributed to the prolonged residence time of CO and H_2O at high concentrations in the CLG system, which promotes the forward reaction of R7, resulting in higher CO_2 production. However, this increase in CO_2 cannot be efficiently mitigated due to the diminished concentration of CaO in the upper regions of the gasifier. Consequently, it can be deduced that the gasifier height will profoundly influence the thermochemical behaviors in the CLG process. Although increasing the gasifier height may enhance fuel conversion and hydrogen production, it can adversely affect the efficiency of CO_2 absorption.

Fig. 9 illustrates the axial pressure drop distribution in the gasifier of the CLG system with different riser heights. It is evident that increasing the height of the riser results in a greater pressure drop between the reactor inlet and outlet. This observation is aligned with precious experimental findings, indicating that the additional energy requirement to transport solid materials to the gasifier outlet is a consequence of increasing the reactor height.

4.4. *Influence of gasifier diameter on the CLG process*

The internal diameter of gasifier plays a critical role in shaping the hydrodynamic and thermochemical characteristics of CLG process. Yan et al. (2004) experimentally investigated the effect of the internal diameter of riser on the axial and radial distribution of solid holdup in the cold gas–solid flow. It was indicated that the concentration of solid particles increases with the riser diameter, and the radial distribution of solid holdup is steeper in the riser with a larger diameter. Furter investigations revealed that larger-diameter riser exhibits a reduced cross-sectional average particle velocity. Additionally, particle velocities show

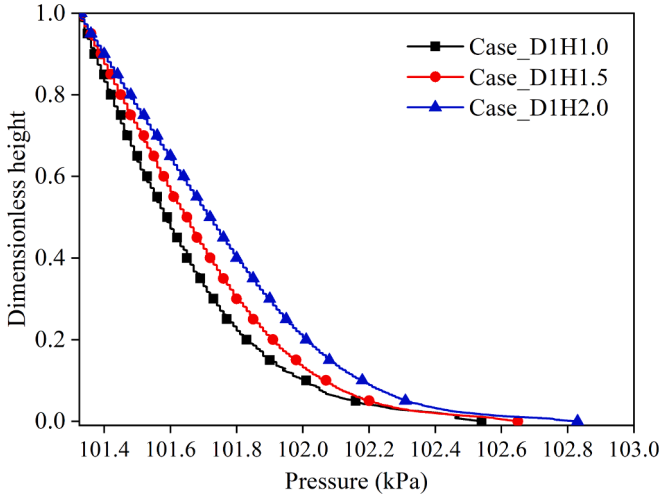

Fig. 9. Pressure distributions in the gasifiers with different heights.

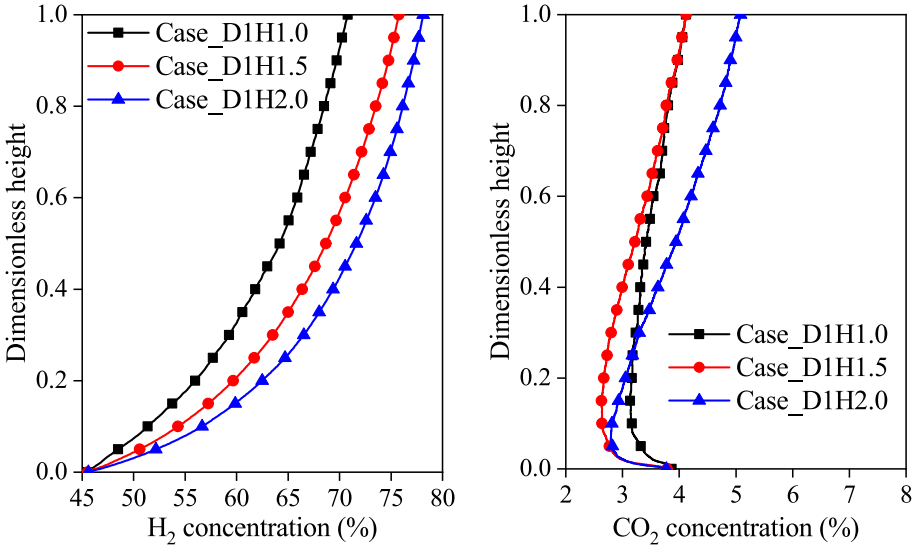

Fig. 8. Axial distribution of H_2 and CO_2 concentrations in gasifier with different heights.

minimal variance in the core regions of risers regardless of diameter, whereas near the walls, smaller-diameter risers display significantly higher particle velocities (Yan and Zhu, 2005). Moreover, they examined the effect of riser diameter on the axial and radial solid flux in three sets of risers with different diameters, finding that the radial distribution of solid flux in larger-diameter riser is more non-uniform compared to those with smaller diameters (Yan et al., 2005). These studies have highlighted the internal diameter of the riser as a pivotal role affecting the gas–solid flow dynamics. In pursuit of providing theoretical insights for the configuration optimization of gasifier diameter in the CLG system, the influence of riser internal diameter on the thermochemical characteristics is deeply delved in the current simulation. Extending from previously described experimental setups, three different riser configurations featuring with internal diameter at 0.5, 1.2 and 1.5 times of the experimental benchmark are numerically discussed in the current investigation. The specific dimensions of these cases are listed in Table 10. To further analyze the impact of reactor diameter on the CLG process, the height-to-diameter ratio is employed as a dimensionless parameter for comparison. Given the objective of this study is to examine the influence of riser reactor internal diameter on CLG performance under consistent operational conditions, the initial static height of bed materials is kept the same across different scenarios. Moreover, the molar ratios of calcium to carbon and steam to carbon are maintained consistent with the experimental setups.

Fig. 10 presents the time-averaged molar fraction of gas species at the gasifier outlet with different height-to-diameter ratios. It can be observed that under conditions of constant riser reactor height, there exists an optimal internal diameter that yields the highest concentration of H_2 in the CLG products. Furthermore, as the internal diameter of gasifier increases, there is a noticeable trend of diminishing CH_4 concentrations, whereas the variation in CO concentration is not particularly pronounced across different configurations. Importantly, at an internal diameter of 0.1 m in the current simulation, there is a remarkable deterioration in the CO_2 absorption efficiency. Under the specific conditions of our current simulation, it is suggested that a height-to-diameter ratio of 28.8 achieves the optimal configuration for the gasifier in the coal-fueled CLG system, enhancing the production of H_2 while also maintaining effective CO_2 absorption. Additionally, the recommended ratio of 28.8 is consistent with the design of the fuel reactor in our previous studies on a 1 MW_{th} pilot-scale coal-fueled CLC system (Lin et al., 2022a).

Fig. 11 illustrates the time evolutions of the void fraction in the gasifier of the CLG process with different height-to-diameter ratios. The non-uniform structures become quite apparent in the riser reactor with excessively small internal diameter. Due to the reduced diameter, these non-uniform structures near the reactor walls are closely spaced, which is detrimental to the flow dynamics in the CLG process. For this reason, the lowest H_2 yield is obtained in the gasifier outlet with a height-to-diameter ratio of 69.7 during the coal-based CLG process. On the other hand, the non-uniform structures with elongated cluster can be observed in the riser with a relatively larger diameter, such as the case with a height-to-diameter ratio of 23 in the current simulation. These formations are unfavorable for gas–solid interaction efficiency in the CLG system. Nevertheless, for the configuration with a height-to-diameter ration of 28.8, fewer non-uniform structures are observed in the gasifier, particularly resulting in a more uniform gas–solid concentration distribution in the upper regions of the riser reactor.

Table 10
Dimensions of gasifiers in the CLG system with different inner diameters.

Case	Diameter (m)	Height (m)	Height-to-diameter ratio
Case_D0.5H1	0.033	2.3	69.7
Case_D1.0*H*1	0.066	2.3	34.9
Case_D1.2H1	0.08	2.3	28.8
Case_D1.5H1	0.1	2.3	23.0

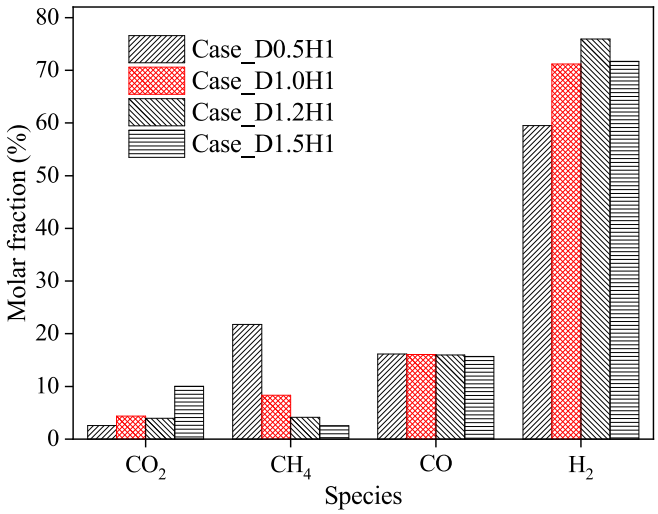

Fig. 10. Gas species mole fraction at the outlet of gasifiers with different diameters.

Fig. 12 displays the radial distribution of solid concentrations in the middle and upper regions of the riser reactor with different height-to-diameter ratios. It can be observed that in the gasifier with smaller diameters, the solid concentration exhibits a “V” shape distribution. For height-to-diameter ratios of 34.9 and 28.8, the radial distribution of solid concentration follows a parabolic curve, whereas in the gasifier with larger diameters, the concentration pattern takes on a “W” shape distribution.

The pressure drop distribution in the fluidized bed represents a crucial parameter, reflecting the system energy consumption and providing insights into the fluidization and disturbance performances during the CLG process. Fig. 13 quantitatively depicts the time evolution profiles and time averaged distributions of pressure drop for configurations with different height-to-diameter ratios. Due to the startup effect, the pressure drop in the gasifier initially increases, followed by a gradual decrease, and eventually stabilizes, fluctuating around a constant value. Notably, the configuration with a height-to-diameter ratio of 69.7 displays a distinct transient pressure drop with significantly higher fluctuation amplitude compared to other cases, underscoring the intense gas–solid disturbance in the riser reactor with smaller inner diameter due to the presence of numerous non-uniform structures. The axial distributions reveal that the pressure drop in gasifier with smaller diameters is significantly higher than in others, which is related to the dense arrangement of non-uniform structures adjacent to the riser walls. Furthermore, the riser reactor featuring a height-to-diameter ratio of 28.8 presents the lowest pressure drop between the gasifier inlet and outlet among all investigated configurations, suggesting that the optimal gas–solid flow condition has been achieved.

Fig. 14 shows the time evolutions of solid flux in the gasifiers with different internal diameter after reaching a dynamic steady state. It is evident that the riser reactor with the smallest internal diameter exhibits a notably higher solid flux compared to reactors under other configurations, indicating excessively rapid gas–solid flow. This rapid flow shortens the residence time of solid fuel and absorbent in the CLG system, resulting in a decreased gas–solid interaction efficiency and a reduced fuel conversion rate. The configuration with a height-to-diameter of 23 demonstrates significant fluctuations in solid flux, indicating the non-uniform gas–solid mixing behavior due to the elongated clusters in the gasifier. Additionally, the solid flux in the gasifier with a height-to-diameter of 28.8 shows smaller fluctuations and is slightly beneath that presented in the original experimental setup. This suggested that the proposed configuration with a height-to-diameter ratio of 28.8 facilitates more uniform and sufficient gas–solid interactions.

Fig. 11. Instantaneous contour plots of void fraction in the risers with different diameters.

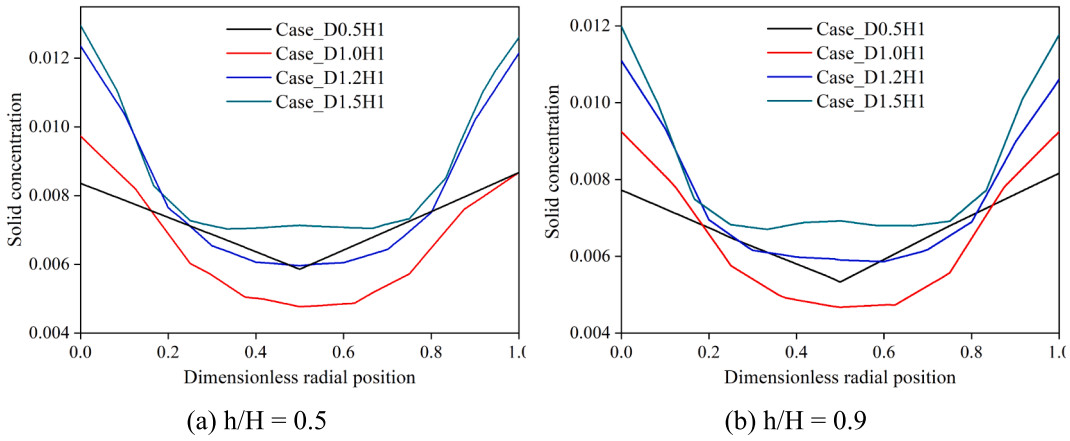

Fig. 12. Radial distribution of solid concentration in risers with different inner diameters.

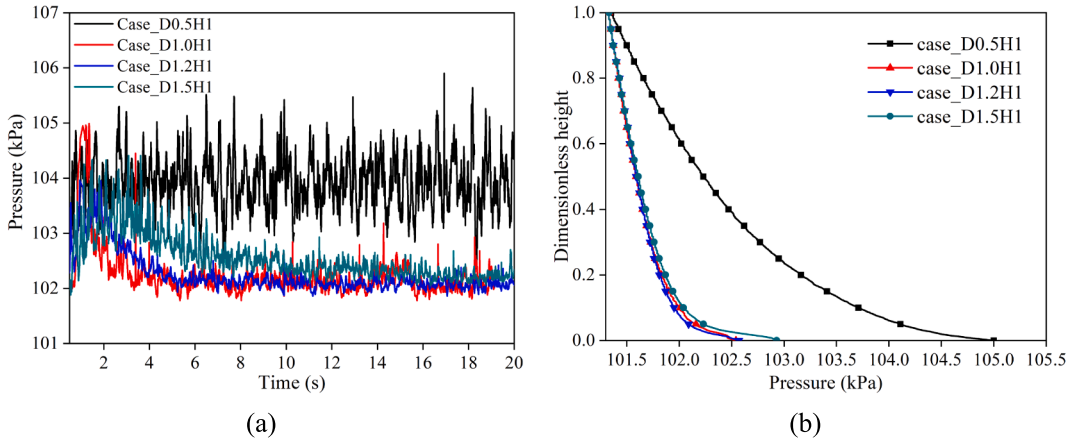

Fig. 13. Pressure drops in gasifiers with different inner diameters: (a) transient distribution; (b) axial distribution.

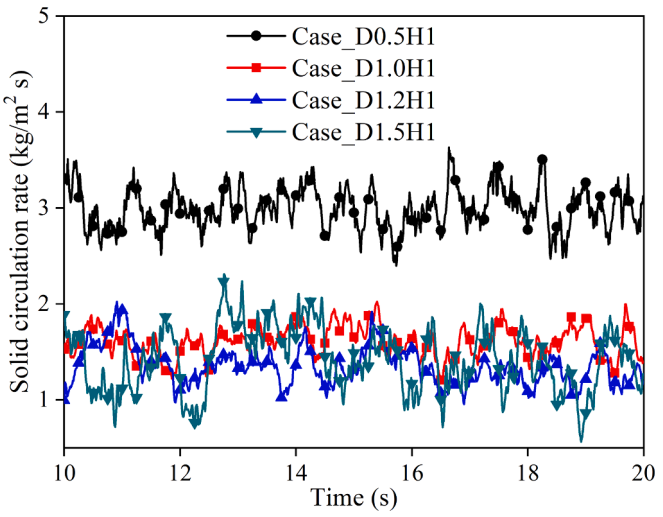

Fig. 14. Solid flux in gasifiers with different diameters.

The granular temperature can be utilized to characterize the fluctuation of solid velocity in the CLG system. Fig. 15 presents the radial distribution of granular temperature in the gasifiers with different height-to-diameter ratios. A largest solid granular temperature manifesting in a parabolic distribution is displayed in the riser reactor with the largest height-to-diameter ratio, which indicates particularly pronounced gas–solid fluctuations in this configuration. On the contrary, the "M" shape solid granular temperature distributions with the lowest values near the wall regions can be observed in the other configurations, which is related to the back-mixing phenomena of particles near the walls. Moreover, the granular temperature in the central regions of the risers is lower than the surrounding areas due to the relatively low solid concentration and similar upward solid motions. Furthermore, the riser reactor with larger internal diameters exhibits significant fluctuations in the solid granular temperature, likely attributed to the unstable gas–solid flow induced by elongated cluster structures.

4.5. *Influence of superficial gas velocity on the CLG process*

Finally, the influence of superficial gas velocity on the performance of hydrogen production and carbon reduction in the CLG process is investigated based on Case_D1.2H1. Four sets of operating conditions are established with superficial velocities of 0.48 m/s, 0.64 m/s, 0.8 m/s, and 0.96 m/s. The gas product yields, coal particle reaction time, and the variation in coal particle size over time are quantitatively analyzed at different gas velocities. Fig. 16(a) presents the time-averaged molar concentrations of CO_2 and H_2 at the gasifier outlet under different superficial velocities. It can be observed that with increasing gas flow rate, the H_2 concentration in the CLG process slightly decreases while the CO_2 concentration increases. However, the overall changes in H_2 and CO_2 concentrations are minimal, indicating that the impact of superficial gas velocity on the purity of the gas products in the CLG process is negligible. This finding is consistent with conclusions drawn from previous studies (Wang et al., 2018a). Fig. 16(b) illustrates the H_2 and CO_2 mass flow rates in the CLG process with varying superficial velocities. Interestingly, as the gas velocity increases, the mass flow rates of both H_2 and CO_2 initially decrease and then increase. This phenomenon can be attributed to the fact that as the gas velocity increases, the residence time of solids in the CLG reactor decreases, leading to a reduction in coal particle reaction time and, consequently, a slight decrease in H_2 yield. However, further increases in gas velocity improve particle mixing and gas–solid heat transfer, ultimately boosting H_2 yield. For CO_2, at low superficial gas velocities, the inadequate mixing of absorbent particles leads to insufficient removal of CO_2 from the reactor, resulting in higher CO_2 flux. At high gas velocities, the reduced residence time of absorbent particles in the reactor also diminishes CO_2 absorption efficiency. Therefore, the superficial gas velocity has a multifaceted influence on the hydrogen production and carbon reduction performance in the CLG process, necessitating a comprehensive consideration of its effects on fuel reaction time, gas–solid interactions, and other factors.

Leveraging the inherent advantages of the proposed model in tracking individual parcels, Fig. 17 presents the probability density function distribution of solid residence times (SRT) for coal particles in the gasifier with different gas velocities. It is observed that the residence time of coal particles in the gasifier decreases with increasing gas velocity, exhibiting a characteristic "early peak and long tail" distribution. Quantitatively, the average reaction times of coal particles in the gasifier are 1.42 s, 1.27 s, 1.15 s, and 1.07 s at gas velocities of 0.48 m/s, 0.64 m/s, 0.8 m/s, and 0.96 m/s, respectively. This finding quantitatively explains the initial decrease in H_2 flow rate as gas velocity increases.

In the current simulation, the shrinking particle size model is employed to calculate heterogeneous chemical reactions, wherein the particle size is adjusted with mass changes while maintaining constant density. Fig. 18 quantitatively tracks the time evolution of the average coal particle size in the CLG system with different superficial gas velocities. Initially, the coal particles rapidly decrease in size as the reaction proceeds, eventually stabilizing and fluctuating around a near-steady-state value. The numerical results indicate that higher superficial velocities in the gasifier result in larger average coal particle sizes due to the reduced reaction time of coal particle, as shown in Fig. 17. Additionally, it demonstrates that excessively high or low gas velocities lead to increased fluctuations in average coal particle size, causing a broader particle size distribution. This variability negatively impacts

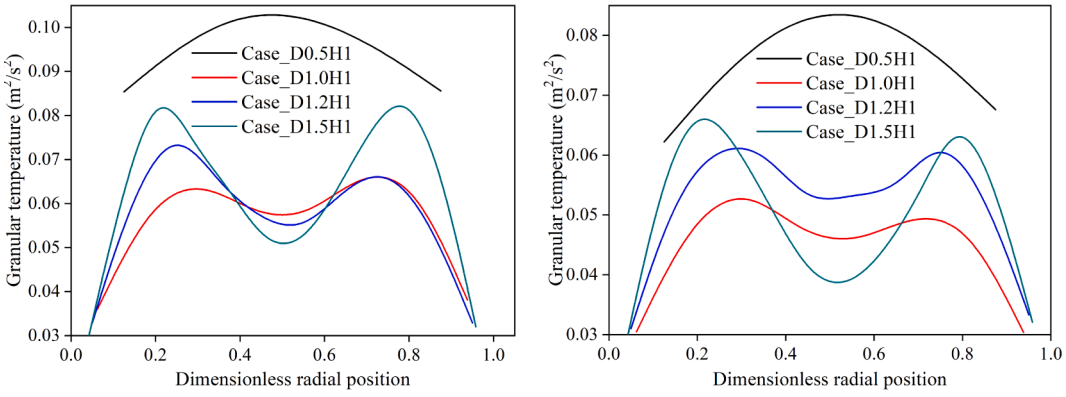

Fig. 15. Radial distribution of granular temperature in gasifiers with different diameters.

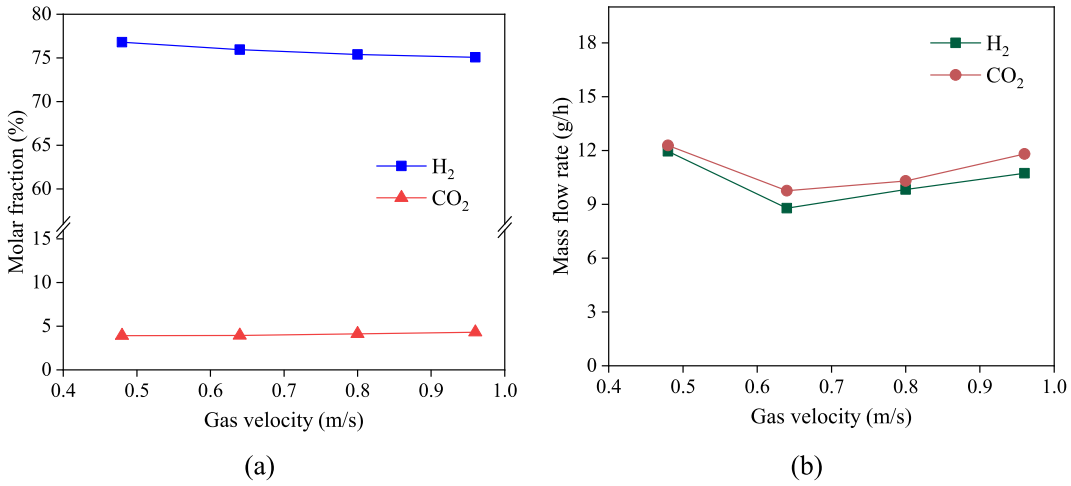

Fig. 16. Influence of gas velocity on product gas species: (a) H_2 and CO_2 molar concentrations; (b) H_2 and CO_2 mass flow rates.

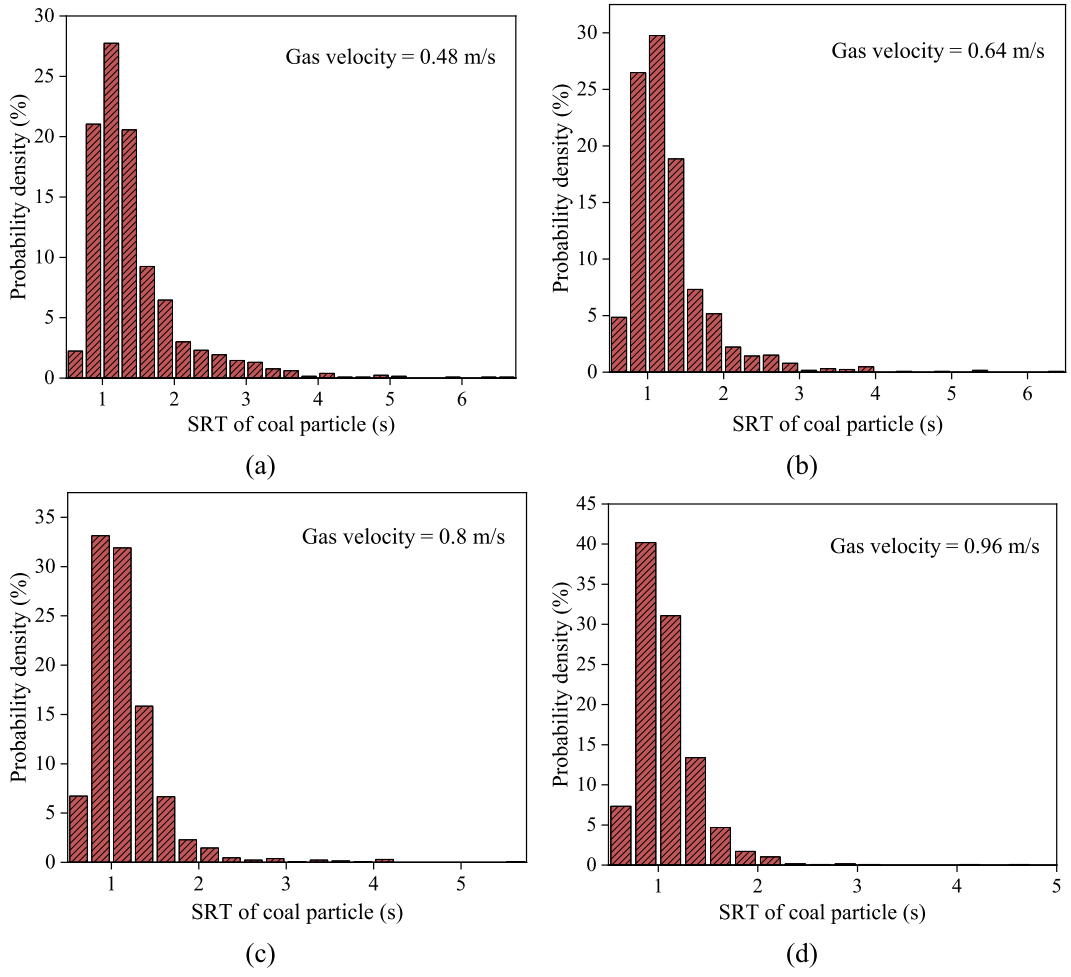

Fig. 17. Coal particle residence times in the gasifier with different gas velocities: (a) 0.48 m/s; (b) 0.64 m/s; (c) 0.8 m/s; (d) 0.96 m/s.

particle mixing and reaction uniformity, ultimately diminishing the hydrogen production and carbon capture efficiency in the CLG system.

5. Conclusions

A coarse-grained method has been implemented into the reactive CFD-DEM framework to boost the computational efficiency for the simulations of coal-based CLG process in 3D riser reactors. Specifically, the polydispersity effect in gas–solid momentum exchange, inter-particle contacts, comprehensive heat transfer mechanisms, homogeneous and heterogeneous chemical reactions during the CLG process are thoroughly considered in the proposed approach. Firstly, the model developed in this study is validated against experimental measurements, followed by independence analysis concerning the coarse-grained ratio

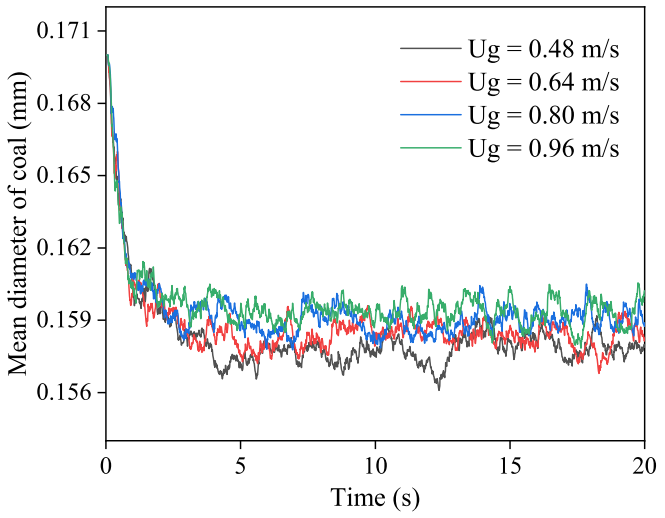

Fig. 18. Time evolution of the average coal particle size in the gasifier with different gas velocities.

and grid resolution. Subsequently, numerical investigations about the gasifier configuration optimization in the CLG system are conducted, focusing on the influences of riser reactor height and diameter on the hydrodynamics and thermochemical performance in the CLG process.

The height and internal diameter of the gasifier in the CLG system significantly influence its hydrogen production and carbon reduction characteristics. Increasing the height of gasifier extends the residence time of solid fuel in the CLG system, leading to a higher fuel conversion efficiency and yielding a higher concentration of gasification product H_2 at the reactor outlet. Nevertheless, this also prolongs the duration for homogeneous reactions in the CLG system, resulting in an increased CO_2 concentration due to WGS reaction. Moreover, an increase in riser height leads to a decreased content of CaO sorbent in the upper regions, hindering efficient CO_2 absorption and removal. When the height of riser reactor remains constant, variations in its internal diameter markedly influence the CLG performance. Specifically, smaller diameters cause an excessively rapid gas–solid flow and shorten the residence time for solid fuel, leading to incomplete fuel conversion. On the one hand, the closely packed non-uniform structures in the smaller-diameter gasifier increase the energy consumption for gas–solid transport and adversely affect the gas–solid interactions in the CLG process. On the other hand, the presence of elongated cluster structures in the riser reactor with larger diameter leads to dramatically fluctuations of gas–solid flow, significantly deteriorating hydrogen production and carbon absorption performance in the CLG process. Consequently, based on the current simulation findings, the optimal height-to-diameter ratio for the gasifier in a CLG system is approximately 28.8, optimizing H_2 production while maintaining efficient CO_2 absorption. Additionally, the superficial gas velocity has a multifaceted influence on the hydrogen production and carbon reduction performance in the CLG process, necessitating a comprehensive consideration of its effects on fuel reaction time, gas–solid interactions, and other factors.

In summary, this study aims to lay a solid foundation for the commercial application of CLG technology, pioneering innovative techniques for the clean, efficient, and low-carbon utilization of coal energy. As a foundational implementation, the current numerical investigation ensures a robust examination of hydrogen production and carbon reduction behavior in the CLG reactors with different height-to-diameter ratios. However, solid-fueled CLG is a complex multiphysics coupled process characterized by strong nonlinear interactions among gas–solid flow, heat and mass transfer, and chemical reactions. Future research will expand on this work by exploring the coupling effects between various operating parameters and gas–solid hydrodynamics and thermochemical performance. Future investigation will also include 3D full-loop simulations of the CLG process in a dual-circulating fluidized bed system, with a focus on the integrated influence of the coupling effects of gasifier and combustor on the bed material circulation, solid residence time, coal gasification, absorbent absorption and regeneration behaviors. Furthermore, it should be noted that the recommended height-to-diameter ratio of 28.8 may not be universally applicable to different operational scenarios. Further investigations are necessary to extend our current findings to other dense gas–solid reacting flows. By addressing these aspects, more holistic perspectives on the practical design, optimization, and commercial application of CLG technology will be brought to light.

CRediT authorship contribution statement

Junjie Lin: Writing – review & editing, Writing – original draft, Visualization, Validation, Methodology, Investigation. **Kun Luo:** Supervision, Project administration, Funding acquisition, Conceptualization. **Shuai Wang:** Writing – review & editing, Visualization, Software, Formal analysis, Data curation. **Jianren Fan:** Writing – review & editing, Supervision, Project administration, Formal analysis, Conceptualization.

Declaration of competing interest

The authors declare that they have no known competing financial interests or personal relationships that could have appeared to influence the work reported in this paper.

Data availability

Data will be made available on request.

Acknowledgments

The authors thank the financial support from the National Natural Science Foundation of China (grant No. 51925603) and the Postdoctoral Fellowship Program of CPSF (GZB20230625).

References

Abdelmotalib, H.M., Youssef, M.A., Hassan, A.A., Youn, S.B., Im, I.-T., 2015. Heat transfer process in gas–solid fluidized bed combustors: A review. Int. J. Heat Mass Transf. 89, 567–575.

Abuelgasim, S., Wang, W., Abdalazeez, A., 2021. A brief review for chemical looping combustion as a promising CO2 capture technology: Fundamentals and progress. Sci. Total Environ. 764, 142892.

Baker, E., 1962. 87. The calcium oxide–carbon dioxide system in the pressure range 1–300 atmospheres. J. Chem. Soc. Resumed, 464–470.

Batchelor, G.K., O'Brien, R.W., 1977. Thermal or Electrical Conduction Through a Granular Material. Proceedings of the Royal Society A: Mathematical, Physical and Engineering Sciences 355, 313-333.

Baum, M.M., Street, P.J., 1971. Predicting the Combustion Behaviour of Coal Particles. Combust. Sci. Technol. 3, 231–243.

Beetstra, R., van der Hoef, M.A., Kuipers, J.A.M., 2007a. Drag force of intermediate Reynolds number flow past mono- and bidisperse arrays of spheres. AIChE J 53, 489–501.

Beetstra, R., van der Hoef, M.A., Kuipers, J.A.M., 2007b. Numerical study of segregation using a new drag force correlation for polydisperse systems derived from lattice-Boltzmann simulations. Chem. Eng. Sci. 62, 246–255.

Bryden, K.M., Ragland, K.W., Rutland, C.J., 2002. Modeling thermally thick pyrolysis of wood. Biomass Bioenergy 22, 41–53.

Cai, J., Wang, S., Zeng, R., Luo, M., Tang, X., 2018. CaO-based chemical looping gasification of biomass for the production of hydrogen-enriched gas and CO 2 negative emissions: a review. International Journal of Energy for a Clean Environment 19.

Chen, L., Yang, L., Liu, F., Nikolic, H.S., Fan, Z., Liu, K., 2017. Evaluation of multi-functional iron-based carrier from bauxite residual for H2-rich syngas production via chemical-looping gasification. Fuel Process. Technol. 156, 185–194.

Dymala, T., Wang, S., Jarolin, K., Song, T., Shen, L., Dosta, M., Heinrich, S., 2022. MP-PIC simulation of biomass steam gasification using ilmenite as an oxygen carrier. Atmos. 13, 1009.

El-Emam, M.A., Zhou, L., Shi, W., Han, C., Bai, L., Agarwal, R., 2021. Theories and applications of CFD–DEM coupling approach for granular flow: A review. Arch. Comput. Meth. Eng. 1–42.
Fang, F., Li, Z.-S., Cai, N.-S., 2009. Experiment and modeling of CO2 capture from flue gases at high temperature in a fluidized bed reactor with Ca-based sorbents. Energy Fuel 23, 207–216.
Golshan, S., Sotudeh-Gharebagh, R., Zarghami, R., Mostoufi, N., Blais, B., Kuipers, J., 2020. Review and implementation of CFD-DEM applied to chemical process systems. Chem. Eng. Sci. 221, 115646.
Gunn, D.J., 1978. Transfer of heat or mass to particles in fixed and fluidised beds. Int. J. Heat Mass Transf. 21, 467–476.
Han, J., Li, J., Tang, X., Wang, L., Yang, X., Ge, Z., Yuan, F., 2023. Coal-fired power plant CCUS project comprehensive benefit evaluation and forecasting model study. J. Clean. Prod. 385, 135657.
Hu, C., Luo, K., Wang, S., Junjie, L., Fan, J., 2019a. The effects of collisional parameters on the hydrodynamics and heat transfer in spouted bed: A CFD-DEM study. Powder Technol. 353, 132–144.
Hu, C., Luo, K., Wang, S., Sun, L., Fan, J., 2019b. Influences of operating parameters on the fluidized bed coal gasification process: A coarse-grained CFD-DEM study. Chem. Eng. Sci. 195, 693–706.
Hu, N., Zhang, H., Yang, H., Yang, S., Yue, G., Lu, J., Liu, Q., 2009. Effects of riser height and total solids inventory on the gas–solids in an ultra-tall CFB riser. Powder Technol. 196, 8–13.
Ismail, M., Liu, W., Dunstan, M.T., Scott, S.A., 2016. Development and performance of iron based oxygen carriers containing calcium ferrites for chemical looping combustion and production of hydrogen. Int. J. Hydrogen Energy 41, 4073–4084.
Jiang, K., Ashworth, P., 2021. The development of Carbon Capture Utilization and Storage (CCUS) research in China: A bibliometric perspective. Renew. Sustain. Energy Rev. 138, 110521.
Kieckhefen, P., Pietsch, S., Dosta, M., Heinrich, S., 2020. Possibilities and limits of computational fluid dynamics–discrete element method simulations in process engineering: A review of recent advancements and future trends. Annual Review of Chemical and Biomolecular Engineering 11, 397–422.
Li, Z., Xu, H., Yang, W., Zhou, A., Xu, M., 2019. CFD simulation of a fluidized bed reactor for biomass chemical looping gasification with continuous feedstock. Energ. Conver. Manage. 201, 112143.
Liang, Y., Zhang, Y., Li, T., Lu, C., 2014. A critical validation study on CPFD model in simulating gas–solid bubbling fluidized beds. Powder Technol. 263, 121–134.
Lin, J., Luo, K., Wang, S., Hu, C., Fan, J., 2020a. An augmented coarse-grained CFD-DEM approach for simulation of fluidized beds. Adv. Powder Technol. 31, 4420–4427.
Lin, J., Luo, K., Wang, S., Sun, L., Fan, J., 2020b. Particle-scale simulation of solid mixing characteristics of binary particles in a bubbling fluidized bed. Energies 13, 4442.
Lin, J., Luo, K., Hu, C., Sun, L., Fan, J., 2022a. Full-loop simulation of a 1 MWth pilot-scale chemical looping combustion system. Chem. Eng. Sci. 249.
Lin, J., Luo, K., Wang, S., Sun, L., Fan, J., 2022b. Particle-scale study of coal-direct chemical looping combustion (CLC). Energy 250, 123859.
Lin, J., Luo, K., Wang, S., Fan, J., 2023. Multi-scale insights of chemical looping combustion in a three-dimensional bubbling fluidized bed. Chem. Eng. J. 474, 145806.
Liu, X., 2023. Low-carbon utilization of coal gangue under the carbon neutralization strategy: a short review. J. Mater. Cycles Waste Manage. 25, 1978–1987.
Lu, L., Xu, J., Ge, W., Yue, Y., Liu, X., Li, J., 2014. EMMS-based discrete particle method (EMMS–DPM) for simulation of gas–solid flows. Chem. Eng. Sci. 120, 67–87.
Lu, L., Konan, A., Benyahia, S., 2017a. Influence of grid resolution, parcel size and drag models on bubbling fluidized bed simulation. Chem. Eng. J. 326, 627–639.
Lu, L., Morris, A., Li, T., Benyahia, S., 2017b. Extension of a coarse grained particle method to simulate heat transfer in fluidized beds. Int. J. Heat Mass Transf. 111, 723–735.
Lu, L., Gao, X., Dietiker, J.-F., Shahnam, M., Rogers, W.A., 2021. Machine learning accelerated discrete element modeling of granular flows. Chem. Eng. Sci. 245, 116832.
Matamba, T., Iglauer, S., Keshavarz, A., 2022. A progress insight of the formation of hydrogen rich syngas from coal gasification. J. Energy Inst. 105, 81–102.
Mohamed, U., Zhao, Y., Huang, Y., Cui, Y., Shi, L., Li, C., Pourkashanian, M., Wei, G., Yi, Q., Nimmo, W., 2020. Sustainability evaluation of biomass direct gasification using chemical looping technology for power generation with and w/o CO2 capture. Energy 205, 117904.
Mori, Y., Sakai, M., 2021. Visualization study on the coarse graining DEM for large-scale gas–solid flow systems. Particuology 59, 24–33.
Rong, D., Horio, M., 1999. DEM simulation of char combustion in a fluidized bed. In: Second International Conference on CFD in the Minerals and Process Industries CSIRO, pp. 65–70.
Sakai, M., Abe, M., Shigeto, Y., Mizutani, S., Takahashi, H., Viré, A., Percival, J.R., Xiang, J., Pain, C.C., 2014. Verification and validation of a coarse grain model of the DEM in a bubbling fluidized bed. Chem. Eng. J. 244, 33–43.
Shen, C., Guo, T., Hu, X., Guo, Q., 2023. Multiphase Particle-in-Cell (MP-PIC) Simulation on Fluidization and Reaction Characteristics in an 80 kW Chemical Looping Gasification Unit. Fine Chemical Engineering 125–146.
Udomsirichakorn, J., Salam, P.A., 2014. Review of hydrogen-enriched gas production from steam gasification of biomass: the prospect of CaO-based chemical looping gasification. Renew. Sustain. Energy Rev. 30, 565–579.
Wang, Z., Ku, X., Lin, J., 2024. Three-Dimensional Full-Loop Simulation of Gas-Solid Flow Behaviors in a Chemical Looping Gasification System with a Two-Staged Fuel Reactor. Energy Fuel 38, 4244–4255.
Wang, S., Shen, Y., 2022. Coarse-grained CFD-DEM modelling of dense gas-solid reacting flow. Int. J. Heat Mass Transf. 184.
Wang, S., Luo, K., Hu, C., Sun, L., Fan, J., 2018a. Impact of operating parameters on biomass gasification in a fluidized bed reactor: An Eulerian-Lagrangian approach. Powder Technol. 333, 304–316.
Wang, S., Yin, W., Li, Z., Yang, X., Zhang, K., 2018b. Numerical investigation of chemical looping gasification process using solid fuels for syngas production. Energ. Conver. Manage. 173, 296–302.
Wang, S., Luo, K., Fan, J., 2020. CFD-DEM coupled with thermochemical sub-models for biomass gasification: Validation and sensitivity analysis. Chem. Eng. Sci. 217, 115550.
Wang, Y., Niu, P., Zhao, H., 2019. Chemical looping gasification of coal using calcium ferrites as oxygen carrier. Fuel Process. Technol. 192, 75–86.
Wang, Q., Rong, N., Fan, H., Meng, Y., Fang, M., Cheng, L., Cen, K., 2014. Enhanced hydrogen-rich gas production from steam gasification of coal in a pressurized fluidized bed with CaO as a CO2 sorbent. Int. J. Hydrogen Energy 39, 5781–5792.
Wang, C., Zhu, J., 2016. Developments in the understanding of gas–solid contact efficiency in the circulating fluidized bed riser reactor: A review. Chin. J. Chem. Eng. 24, 53–62.
Wei, X., Yang, J., Zhu, J., 2020. Experimental analysis of phase segregation in gas-solid circulating fluidized bed riser with direct image calibration. Chem. Eng. J. 379, 122301.
Xie, Z., Shen, Y., Takabatake, K., Yamaguchi, A., Sakai, M., 2020. Coarse-grained DEM study of solids sedimentation in water. Powder Technol. 361, 21–32.
Yan, A., Ball, J., Zhu, J.J., 2005. Scale-up effect of riser reactors (3) axial and radial solids flux distribution and flow development. Chem. Eng. J. 109, 97–106.
Yan, A., Zhu, J., 2004. Scale-up effect of riser reactors (1): axial and radial solids concentration distribution and flow development. Ind. Eng. Chem. Res. 43, 5810–5819.
Yan, A., Zhu, J., 2005. Scale-up effect of riser reactors: Particle velocity and flow development. AIChE J 51, 2956–2964.
Yu, J., Lu, L., Gao, X., Xu, Y., Shahnam, M., Rogers, W.A., 2020. Coupling reduced-order modeling and coarse-grainedCFD-DEMto accelerate coal gasifier simulation and optimization. AIChE Journal 67.
Yu, J., Lu, L., Xu, Y., Gao, X., Shahnam, M., Rogers, W., 2021. Coarse-Grained CFD-DEM Simulation and the Design of an Industrial-Scale Coal Gasifier. Ind. Eng. Chem. Res. 61, 866–881.
Yue, M., Lambert, H., Pahon, E., Roche, R., Jemei, S., Hissel, D., 2021. Hydrogen energy systems: A critical review of technologies, applications, trends and challenges. Renew. Sustain. Energy Rev. 146.